

# SparkJet characterizations in quiescent and supersonic flowfields

T. Emerick · M. Y. Ali · C. Foster · F. S. Alvi · S. Popkin

Received: 27 June 2014 / Revised: 1 November 2014 / Accepted: 5 November 2014 / Published online: 19 November 2014  
© Springer-Verlag Berlin Heidelberg 2014

**Abstract** The aerodynamic community has studied active flow control actuators for some time, and developments have led to a wide variety of devices with various features and operating mechanisms. The design requirements for a practical actuator used for active flow control include reliable operation, requisite frequency and amplitude modulation capabilities, and a reasonable lifespan while maintaining minimal cost and design complexity. An active flow control device called the SparkJet actuator has been developed for high-speed flight control and incorporates no mechanical/moving parts, zero net mass flux capabilities and the ability to tune the operating frequency and momentum throughput. This actuator utilizes electrical power to deliver high-momentum flow with a very fast response time. The SparkJet actuator was characterized on the benchtop using a laser-based microschiere visualization technique and maximum blast wave and jet front velocities of  $\sim 400$  and  $\sim 310$  m/s were, respectively, measured in the flowfield. An increase in jet front velocity from 240 to 310 m/s during subatmospheric (60 kPa) testing reveals that the actuator may have greater control authority at lower ambient pressures, which correspond to high-altitude flight conditions for air vehicles. A SparkJet array was integrated into a flat plate and tested in a Mach 1.5 crossflow. Phase-conditioned shadowgraph results revealed a maximum flow deflection angle of  $5^\circ$  created by the SparkJet

275  $\mu$ s after the actuator was triggered in single-shot mode. Burst mode operation of frequencies up to 700 Hz revealed similar results during wind tunnel testing. Following these tests, the actuator trigger mechanism was improved and the ability of the actuator to be discharged in burst mode at a frequency of 1 kHz was achieved.

## 1 Introduction

Inherent flow instabilities associated with a variety of different flow regimes and conditions can produce adverse effects that lead to a reduction in aerodynamic performance. Unsteady flows due to resonance and other phenomena such as those created by impinging jets and present in cavity flows in weapons and cargo bays can lead to unsteady pressure loads resulting in high noise levels and mechanical fatigue. Shock waves associated with supersonic and hypersonic flowfields create large pressure and temperature gradients that can lead to reductions in engine inlet pressure recovery. Some of these adverse effects may be reduced using flow control actuators that modify the flow to achieve a desired control objective.

Various classes of flow control actuators have proven beneficial for aerodynamic performance by influencing the flowfield. Performance benefits include drag reduction, control of unsteady flow effects, and improvements in fuel mixing. Various active flow control (AFC) devices have been tested in many different flow regimes. Synthetic jets have been successfully implemented for flow control in low-speed flows over airfoils (Glezer and Amitay 2002). Caruana et al. (2013) demonstrate, in low-speed flows, the ability of plasma synthetic jets to reduce the separated flow region on a decelerating ramp and also an airfoil. Wang et al. (2013) present a recent review on the use of dielectric

---

T. Emerick (✉) · M. Y. Ali · C. Foster · F. S. Alvi  
Florida Center for Advanced Aero-Propulsion, Department  
of Mechanical Engineering, FAMU-FSU College of Engineering,  
Florida State University, Tallahassee, FL, USA  
e-mail: tomemerick2@gmail.com

S. Popkin  
Force Projection Department, 11100 Johns Hopkins Road,  
Laurel, MD, USA

barrier discharge (DBD) actuators in various flowfields. Electrokinetic microactuators have also been used for boundary layer control in turbulent flows (Diez-Garias et al. 2000). Steady blowing using high-momentum micro-orifices, referred to as microjets, has been used to delay separation in canonical flows such as the Stratford ramp (Kumar and Alvi 2009) and highly loaded low-pressure turbine blades (Fernandez et al. 2013). AFC devices used in low-speed flows have been characterized extensively and have demonstrated their effectiveness for flow control. AFC devices effective in high-speed flows, however, have proven more challenging and continue to be an active area of research.

Some of the AFC devices tested for high-speed flow control include steady blowing using high-momentum microjets. Steady microjets have successfully demonstrated their efficacy as AFC actuators, effects range from the reduction in unsteadiness in supersonic cavities (Zhuang et al. 2006) and shock wave boundary layer interactions near a compression ramp (Ali et al. 2013) to noise reduction and lift enhancement in impinging jet flowfields (Alvi et al. 2008). Although the effect of steady control has been significant in most applications, research has also demonstrated that pulsed jets (unsteady operation) may produce further enhancements (Ali et al. 2010). Resonance Enhanced Microjet actuators capable of unsteady actuation, production of high-amplitude oscillations, and operation over a large bandwidth with slight modification of the geometry or pressure have been characterized in Mach 1.5 flow over a cavity (Ali et al. 2010) and also over a flat plate (Topolski et al. 2012).

More recently, research has focused on developing plasma actuators for AFC. Plasma actuators are of several different types, namely DBD plasma actuators, Magneto-hydrodynamic plasmas, Localized Arc Filament Plasma Actuators (LAFPA), and SparkJets. Reedy et al. (2013) have characterized a pulsed-plasma jet actuator using both schlieren imaging and particle image velocimetry measurement diagnostics to determine a maximum jet velocity of 496 m/s. The interaction of surface discharge plasma actuators with the boundary layer on a flat plate in a Mach 5 flowfield has been studied by Shang et al. (2008). Gnemmi et al. (2013) have studied a surface discharge plasma actuator for the steering of a projectile in a shock tunnel at a Mach number of 4.5. Magnetically driven surface plasma actuators have been used for flow control in a shock wave induced boundary layer separation in Mach 2.6 and 2.8 flowfields (Kalra et al. 2007, 2009). LAFPA are unsteady actuators with a very wide bandwidth capable of affecting transonic to supersonic jets with Mach numbers ranging from 0.9 to 1.65 (Samimy et al. 2011) and also the interaction of a turbulent boundary layer with an oblique shock wave in a Mach 2.3 flowfield (Webb et al.

2013). Pulsed-plasma jets have also been developed for high-speed flow control and tested in a Mach 3 crossflow (Narayanaswamy et al. 2010) and in a shock wave boundary layer interaction in a Mach 3 flowfield (Narayanaswamy et al. 2012).

For flow control to be widely applicable and practical, the ideal actuator should be capable of performing at frequencies that are naturally present in the base flowfield. For a vast range of high-speed flow regimes and applications, this translates to a need for actuation ranging from several hundred hertz to the tens of kilohertz or even higher. The ideal actuators should also be capable of producing high-amplitude mean (time averaged) flow as well as unsteady perturbations over a large dynamic range. Many existing unsteady actuators do not meet these requirements of producing both a high-amplitude, time-averaged component as well as a significant fluctuating component with frequency modulation—most generally produce one or the other. Under the Air Force Office of Scientific Research sponsorship, Florida State University's Florida Center for Advanced Aero-Propulsion, in collaboration with The Johns Hopkins University Applied Physics Laboratory (JHU/APL), have been investigating the SparkJet actuator that holds the promise of manipulating high-speed flows.

The SparkJet is capable of producing a phase controlled, high-amplitude pulsed jet, a combination that can potentially be used to alleviate some of the adverse aerodynamic effects in a closed loop/feedback implementation. The very short rise time of the SparkJet coupled with the relatively high momentum produced, makes it especially attractive for the control of high-speed flows. Some possible applications may include: the suppression of resonant tones and flow unsteadiness associated with supersonic cavity flows, control of shock induced boundary layer interactions in supersonic inlets and elsewhere, and perhaps even transition control for hypersonic vehicles. Other applications will likely arise as one better understands and improves the properties of flow control actuators such as the SparkJet actuator.

The present manuscript includes the process of developing, analyzing, and improving the SparkJet actuator that was first developed by Grossman et al. (2003) in association with JHU/APL. A variety of SparkJet actuators are presented and subsequently characterized under different test conditions. Parameters such as the number of orifices, orifice diameter, operating frequency, trigger mechanism, and active refill supply pressures were varied during operation in a quiescent flowfield to determine the effect of these parameters on the properties of the flow produced by the actuator. The actuator was subsequently implemented into a flat plate in a Mach 1.5 flowfield and operated in a single-shot and burst mode up to 700 Hz to examine the control authority of the actuator in a high-speed flowfield.

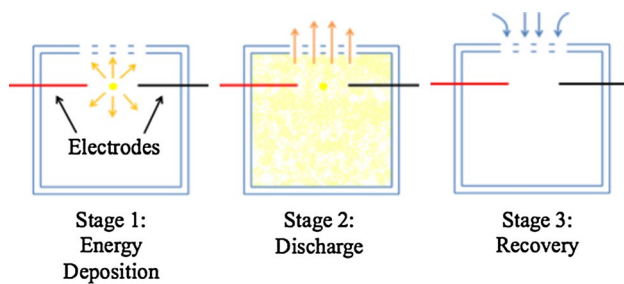


**Fig. 1** SparkJet operating cycle schematic

## 2 SparkJet description and operating modes

The actuator consists of metal electrodes fixed inside a two-part MACOR<sup>®</sup> block consisting of an internal cavity and a lid with exit orifices. The operating cycle of the actuator, as shown in the schematic in Fig. 1, consists of three distinct stages: energy deposition, discharge, and recovery.

During stage one of the operating cycle, the actuator utilizes electrical energy, in the form of a capacitive arc discharge, to increase the temperature of the air inside of the cavity of the actuator. The increase in air temperature leads to an increase in the pressure of the cavity air and results in air being expelled from the orifices of the actuator during stage two. The actuator is refreshed by the surrounding ambient air following the discharge stage of the operating cycle and the sequence is repeated thereafter.

Two methods of initiating the capacitive discharge that drives the actuator have been investigated and compared (Popkin et al. 2013). A trigger is used to initiate the electrical breakdown by ionizing the air between the sustain electrodes. A pseudo-series trigger method using two tungsten sustain electrodes has been found to be 45 % more efficient in the delivery of electrical energy as opposed to an external trigger method using a third copper electrode (Popkin et al. 2013). The pseudo-series trigger mechanism utilizes the anode as the trigger electrode. This design allows for a larger electrode gap distance, which in turn increases the efficiency of the actuator because the spark is in contact with a larger volume of air allowing for an increase in the thermal energy deposition in the working fluid (see Popkin et al. 2013 for details). Results from SparkJet actuators employing an external trigger as well as those utilizing a pseudo-series trigger are presented in later sections of this manuscript. Photographs and schematics of the two trigger mechanisms can be seen in Fig. 2.

The results obtained here and from previous studies (Foster et al. 2011; Haack et al. 2010; Popkin et al. 2013) of the SparkJet actuator are the basis for developing and improving the operating effectiveness, consistency, and efficiency of the actuator. The SparkJet actuators are first characterized during benchtop studies by capturing

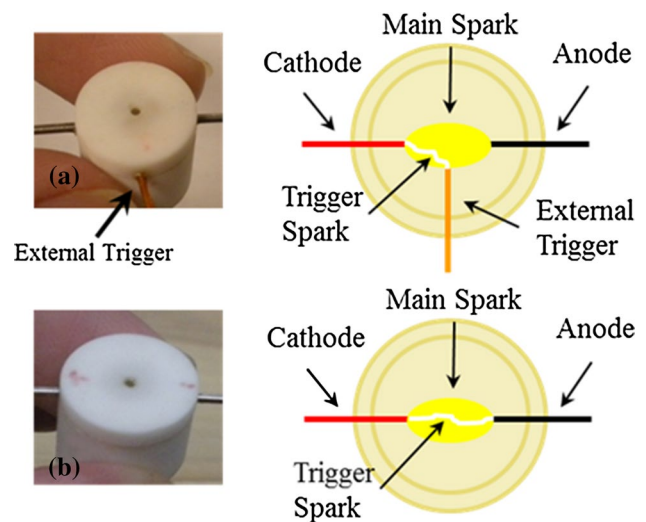


**Fig. 2** Schematics and photographs showing SparkJet trigger mechanisms **a** external trigger (3-electrodes), **b** pseudo-series trigger (2-electrodes)

**Table 1** Actuator design parameters

Actuator design	Orifice diameter (mm)	Number of orifices	Capacitance ( $\mu\text{F}$ )
Design 1	1.0	1	13
Design 2	0.4	4	13
Design 3	0.4	4	7
Design 4	0.8	4	7
Design 5	0.4	12	7

phase-locked images of the flowfield created by the actuators using a laser-based microschiieren (LBMS) technique. The parameters affecting SparkJet performance are varied and from these studies, an effective SparkJet actuator can be designed for wind tunnel testing.

Table 1 displays the physical parameters of the different designs of the actuators. All of the actuators examined in this study have a cavity volume of  $356 \text{ mm}^3$  although there is slight variation in the depth, diameter, and lid thickness of the actuators. The electrodes were charged to approximately 600 V during testing, and the capacitance used was 7 or 13  $\mu\text{F}$  depending on the actuator resulting in an input energy of, respectively, 1.26 and 2.34 Joules per pulse. The actuators were operated in a single-shot mode at 1 Hz and also in a burst mode at 500, 700, and maximum frequency of 1,000 Hz for a fixed number of discharges (typically 11 discharges during benchtop tests and 40 discharges during wind tunnel tests). The repetition rate of the discharges is limited due to the necessary time needed for the cavity of the actuator to be refilled by air and limitations of the electronics in the circuitry.

Additional electrical parameters such as the current drawn were not measured during these sets of experiments. Popkin (2014) has obtained current and voltage values for SparkJet circuitries using capacitance values ranging from 0.95 to 4.28  $\mu\text{F}$ . The results obtained from Popkin (2014) reveal that the total energy discharge lasts 9 and 14  $\mu\text{s}$  for capacitance values of, respectively, 0.95 and 4.28  $\mu\text{F}$ . Extrapolating for total energy discharge times using capacitance values of 7 and 13  $\mu\text{F}$  results in total energy discharge times of, respectively, 18 and 27  $\mu\text{s}$ .

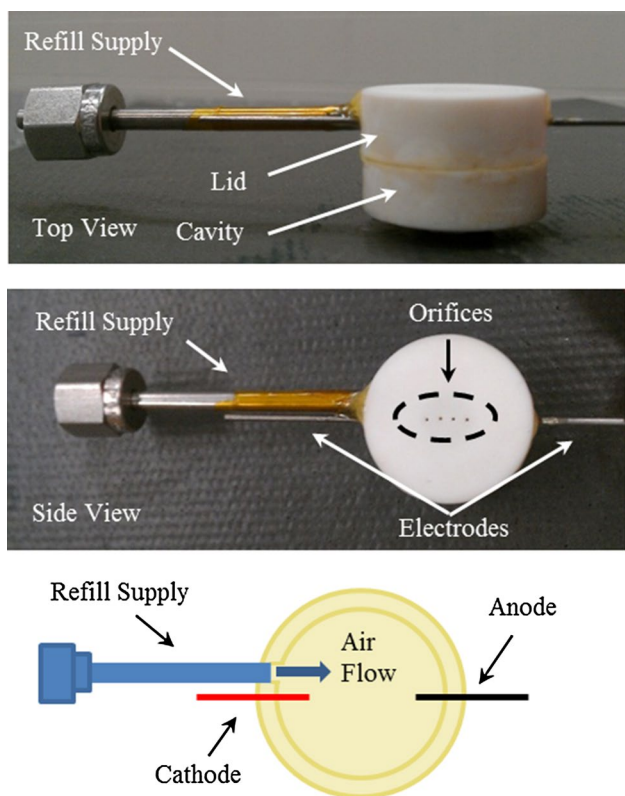


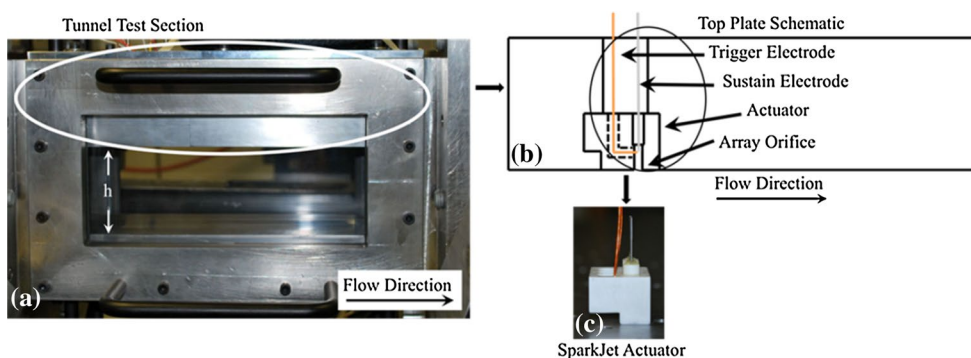
**Fig. 3** Photographs and schematic of SparkJet actuator with cavity refill supply

A nonzero net mass flux (ZNMF) version of the actuator incorporates an active refill supply pressure port as seen in Fig. 3. The lid and cavity of the actuator are also labeled in Fig. 3. This version utilizes compressed air and a Swagelok<sup>®</sup> one-way poppet check valve (not shown in Fig. 3) to supply air to the cavity of the actuator. Air was continually supplied to the cavity during non-ZNMF testing. The refill supply air potentially reduces the refill time of the actuator and may aid in high-frequency testing.

The actuator module used in wind tunnel testing consists of three externally triggered SparkJet assemblies and corresponds to Design 5 in Table 1. Each assembly consists of an electrode set (two parallel tungsten sustain electrodes and a trigger electrode) inside a single 356 mm<sup>3</sup> cavity with four 400- $\mu\text{m}$ -diameter orifices. The resulting array is thus comprised of twelve 400- $\mu\text{m}$  spanwise orifices spaced 2 mm apart (center-to-center). A span of twelve jets, as opposed to a single jet, was chosen to minimize three-dimensional effects. The actuator module was limited to three assemblies due to a lack of electronics to power additional assemblies. The actuator, the three-electrode assemblies, and the location of the actuator in the test section of the wind tunnel can be seen in Fig. 4.

To install the SparkJet array, a single Macor<sup>®</sup> block, Fig. 5, was designed to hold the three-electrode assemblies. Each electrode assembly consists of a cylindrical Macor piece with two axial holes spaced 0.7 mm apart (edge-to-edge) through which the tungsten electrodes slide such that the electrode tips are in the center of the cavity. The actuator used during the wind tunnel tests was externally triggered, and the trigger wire was fed through a small hole in the side of the cavity and secured in place with epoxy. The wind tunnel actuator was externally triggered, as opposed to being triggered by a pseudo-series trigger mechanism, because results from the pseudo-series triggered actuator had not yet been realized by the time the wind tunnel tests occurred. The 12 orifices are oriented normal to the incoming crossflow to allow for a direct comparison to be made to previous studies with steady and unsteady actuators developed at FSU. As a number of our prior studies

**Fig. 4** Actuator location in wind tunnel, **a** tunnel test section, **b** tunnel ceiling, **c** SparkJet actuator



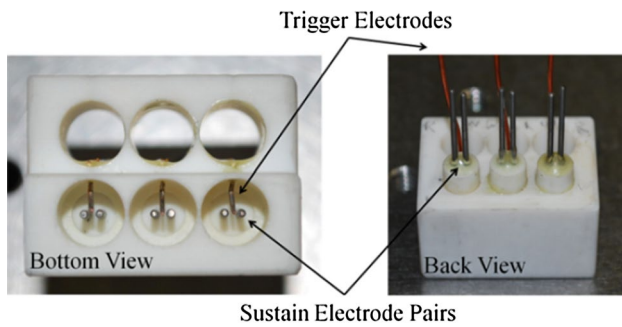


**Fig. 5** Bottom and back views of SparkJet actuator

have shown, the normal orientation of microjets is close to optimal for a number of applications (Zhuang et al. 2006; Kumar and Alvi 2009; Kumar et al. 2011).

### 3 Experimental methods and hardware

#### 3.1 Benchtop characterization

A LBMS system was used to capture phase-locked images of the flowfield created by the actuator. The LBMS system uses a short duration ( $\sim 10$  ns) white light source created by the laser induced breakdown of Argon using a New Wave Gemini PIV laser. The objectives used were plano-convex and have a diameter of 50.8 mm and an f-number of 2.6. A horizontal knife edge was used as the schlieren cut-off to increase the sensitivity of the system. Additional details regarding LBMS can be found in Foster (2011). The experiments were conducted over an extended period of time resulting in modifications being made to the optical equipment between the sets of experiments and therefore direct quantitative comparisons of density gradients are not carried out.

A Nikon objective with a variable focal length of 28–200 mm was used to view the test section and two cameras were used to capture the images, a LaVision Imager ProX, with a resolution of  $1,600 \times 1,200$  pixels, and a Kodak Megaplug ES 1.0, with a pixel resolution of  $1,018 \times 1,008$ . A Stanford Research Systems DG535 delay generator was used to trigger the light source and cameras, and an Agilent 33521A Function/Arbitrary Waveform Generator was used to trigger the SparkJet. The signal sent from the Agilent 33521A Function/Arbitrary Waveform Generator uses a rectangular wave shape in both single-shot and burst operating modes. Phase-locked images of the flowfield created by the actuator were acquired using this hardware.

The time difference between the light source trigger and the SparkJet trigger was varied to capture the temporal evolution of the flowfield. The number of images taken ranged between 12 and 15 images for each set of experiments and

these were then averaged to produce a phase-averaged image from which velocity estimates could be extracted. The displacements of the leading edges of the features from a sequence of images were measured to estimate the velocity. The known time difference between the SparkJet discharge and laser firing, along with a calibration grid used for each experiment with the purpose of defining the pixel per unit length value, was used to estimate the blast wave and jet front velocities. The pixel displacement associated with the motion of the jet front and blast wave was measured by analyzing the images in MATLAB. In the case of the four orifice actuator, the velocity propagations of the blast wave and jet front issuing from the middle left orifice were measured to ensure consistent values. The blast wave and jet front velocities measured from the time-averaged LBMS images have an uncertainty of  $\pm 11$  m/s. This uncertainty is based on the maximum jet front and blast wave thickness in the images and also due to the presence of a small amount of jitter ( $\pm 1$   $\mu$ s) between the trigger spark ionization and the arc discharge initiation.

The actuator with four 400- $\mu$ m-diameter orifices (Design 2 in Table 1) was characterized at ambient atmospheric conditions and also at a subatmospheric pressure of 60 kPa. The actuator was tested at subatmospheric conditions to roughly simulate conditions experienced in the wind tunnel. Although the actual static pressure during the wind tunnel test was  $\sim 35$  kPa, the subatmospheric benchtop tests reveal the effect of reduced pressures on SparkJet performance.

#### 3.2 Wind tunnel characterization

##### 3.2.1 Supersonic wind tunnel

The SparkJet actuator was incorporated into a modular test bed integrated into the wind tunnel ceiling and subsequently tested in a Mach 1.5 crossflow. The supersonic crossflow experiments were conducted at the supersonic wind tunnel facility at the Florida Center for Advanced Aero-Propulsion at Florida State University. The tunnel is supplied with dry, pressurized air from a 10 m<sup>3</sup> air tank at 13 MPa. Control of the air flow to the test section is maintained through the use of two inline valves, a Tescom<sup>TM</sup> dome regulator and a Fisher<sup>TM</sup> control valve. The dome-loading regulator is used for a large drop in pressure from the air tanks and maintains an output pressure of 1.4 MPa. The Fisher control valve is used for the fine control of the tunnel stagnation pressure and is operated from a PC-based LabVIEW data acquisition program. Two inline heaters with a total power of 300 kW, capable of heating the air to 700 Kelvin, are installed to raise the stagnation temperature of the incoming air and prevent condensation in the test section. The test section Mach number can be varied

through the use of interchangeable nozzle blocks. Current experiments were performed at a test section Mach number of 1.5. The run time of the tunnel at these conditions is nominally 90 s. The test section is 305 mm long, 102 mm wide, and 76 mm high, and has optical access from the sides and bottom. The stagnation pressure and temperature are typically maintained at  $138 \text{ kPa} \pm 3 \%$  and  $316 \text{ K} \pm 1 \%$ , respectively. A LabVIEW-based data acquisition program is used to control the wind tunnel and to measure and record the run conditions.

### 3.2.2 Diagnostics

The LBMS system is specifically designed for examining the detailed features of high-speed flows at small ('micro') scales and as such, is mainly used for benchtop studies requiring high spatial resolution. A Z-type focusing shadowgraph system with two parabolic and two  $45^\circ$  mirrors was used instead for wind tunnel flow visualization. The light source used was a white light Xenon flash lamp capable of being pulsed up to a frequency of 1 kHz with a pulse duration of 5–10  $\mu\text{s}$ . While the SparkJet was operating in single-shot mode, a LaVision Imager ProX camera was used with DaVis 7.2 software for image acquisition. The SparkJet, light source, camera, and data acquisition were triggered using a Stanford Research Systems DG-535 delay generator. The time delay between the SparkJet trigger and the light source trigger was varied to capture the temporal evolution of the flow features created by the SparkJet and their effects on the Mach 1.5 flowfield. A minimum number of ten images were taken for each time delay in both single-shot and burst operating modes. The oblique shock angles were measured manually from averaged shadowgraph images with an uncertainty  $\pm 1^\circ$ .

An IDT model Y5 high-speed camera controlled by Motion Studio was used to acquire images during burst mode operation of the SparkJet. Two Stanford Research Systems DG-535 delay generators were used to trigger the data acquisition, light source, camera, and a Strobe Synchronizer frequency divider, at a frequency of 700 Hz. A 1 Hz signal output from the frequency divider was used to trigger an Agilent function generator, which produced a 40 pulse burst at 700 Hz to trigger the SparkJet actuator.

Trigger signals from the function generator and the light source were acquired to monitor jitter in the system which was measured as  $\pm 1 \mu\text{s}$ .

BK Precision Model  $2,000 \times 1,000$  voltage probes were used to measure the voltage across each electrode pair. The voltage across the electrodes decreases nearly instantaneously (O(ns)) when the SparkJet is discharged. This signal was compared with the signal from the light source for measuring the time delay between the arc discharge in the SparkJet and the image acquisition. The signal was also used to confirm the SparkJet discharged reliably during burst mode when the operating frequency is too high to visually confirm the discharge. All signals were simultaneously sampled and acquired using a National Instruments PXI -1031 four slot chassis in combination with a PXI-6133 14-bit eight channel data acquisition card.

## 4 Actuator flow/properties at quiescent conditions (benchtop characterization)

Benchtop testing and characterization of multiple SparkJet actuators was performed to determine how various parameters affect the ability of the actuator to influence high-speed flowfields. The actuator was initially characterized in a single-shot mode at 1 Hz on the benchtop before proceeding on to burst mode operation. Results in this section include phase-locked schlieren images of the flowfield produced by the actuator. Velocity estimates of the blast wave and jet front in the flowfield were obtained through the use of these images. A range of orifice diameters, ambient conditions, refill air supply pressures, discharge frequencies, and trigger mechanisms were tested on the benchtop as shown in Table 2. The cavity volume of all of the actuator assemblies is  $356 \text{ mm}^3$ .

### 4.1 Single-shot operation flow properties

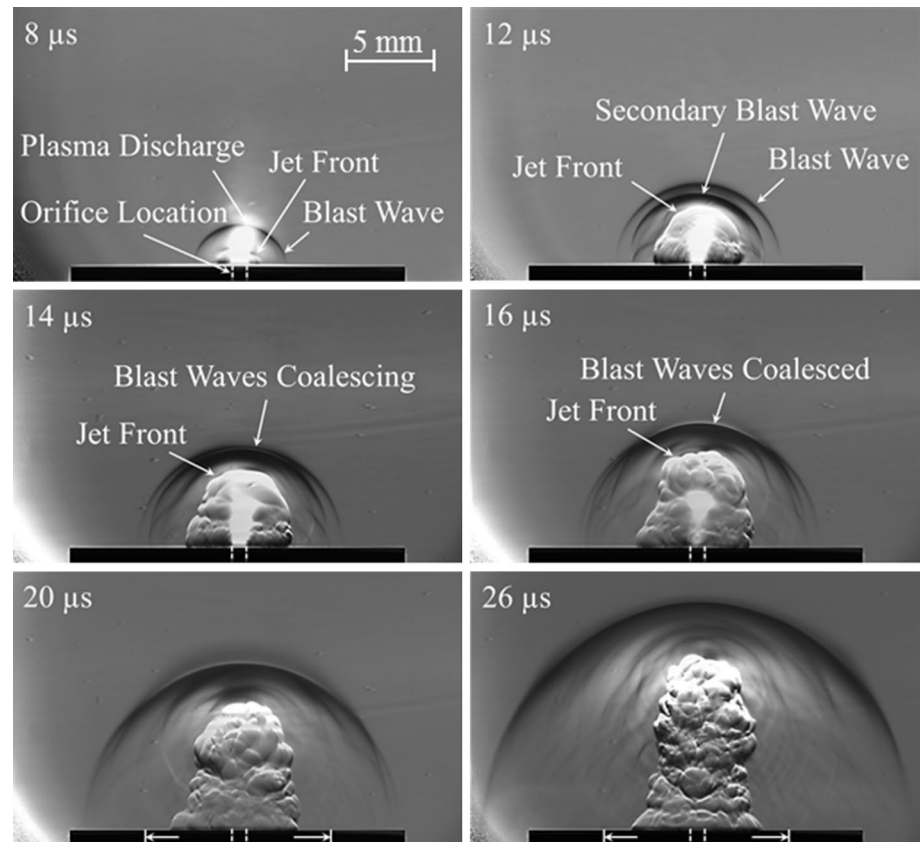
#### 4.1.1 1-mm orifice actuator; atmospheric conditions

Instantaneous phase-locked schlieren images of a single 1-mm orifice SparkJet actuator operating at atmospheric conditions can be seen in Fig. 6. The temporal evolution

**Table 2** SparkJet operating parameters

Parameters	Design 1	Design 2	Design 3	Design 4
Number of orifices	1	4	4	4
Orifice diameter (mm)	1	0.4	0.4	0.8
Ambient conditions (kPa)	101	101, 60	101	101
Refill supply pressure (kPa)	–	–	0, 10, 20	0, 10, 20
Discharge frequency (Hz)	1	1	1, 500, 700, 1,000	1, 500, 700, 1,000
Trigger type	External	External	Pseudo-series	Pseudo-series

**Fig. 6** Time delayed schlieren images of exhaust from single 1 mm orifice externally triggered SparkJet at atmospheric conditions



of the SparkJet flow features were examined by acquiring images where the time delay between the SparkJet arc discharge and the light source trigger was progressively varied. The images shown in Figs. 6, 8, 9, and 10 are of the flowfield created by a SparkJet using an external trigger. The orifice edges are marked by the white dashed lines in all of the schlieren images, and a scale reference of 5 mm is shown on the first image in the series. Many of the principal features have also been marked on this series of images.

The rapid response time of these actuators is confirmed by two key features present in this flowfield, the initial blast wave, and the jet front. These two features can be seen 8  $\mu$ s after the initial discharge. A secondary blast wave can be seen 12  $\mu$ s after the initial discharge. The source of the secondary blast wave is uncertain but may be caused by a reflection of the initial blast wave within the cavity. The secondary blast wave propagates away from the actuator with a velocity greater than the first and coalesces with the initial blast wave 16  $\mu$ s after the SparkJet is discharged. The velocity of the secondary blast wave being greater than the first may be a result of an increase in the local speed of sound due to residual heat from the initial arc inside the cavity.

The thermal plume can be seen in all of the images in Fig. 6 and is believed to be due to the heat transfer from the electrical discharge being conducted through the Macor

actuator lid and convecting into the ambient surrounding air. The actuator lid for these cases has a thickness of 1 mm and an internal cavity diameter of 7.5 mm. The internal diameter of the lid is marked in the images corresponding to time delays of 20 and 26  $\mu$ s by the solid white lines and arrows. The images reveal that the diameter of the thermal plume (5 mm) is slightly smaller than the internal lid diameter (7.5 mm) but much larger than the orifice diameter (1 mm).

A bright white feature is seen just above the orifice in images corresponding to time delays between 8 and 16  $\mu$ s, and this is suspected to be the plasma discharge due to the electrical breakdown between the SparkJet electrodes. This bright feature may also be due to the very high temperatures associated with the discharge flow at early phases; such high temperatures would result in very high density gradients thus saturating the schlieren image where the cut-off is optimized for the overall flowfield. At this point, the precise nature and properties of this feature are unclear and referring to it as plasma may not be exactly accurate; however, we use this term here to distinguish this flow feature from others. The images corresponding to time delays of 20 and 26  $\mu$ s show the propagation of the jet front and coalesced blast wave away from the actuator.

The blast wave and jet front propagation velocities are estimated and plotted versus the time after discharge in

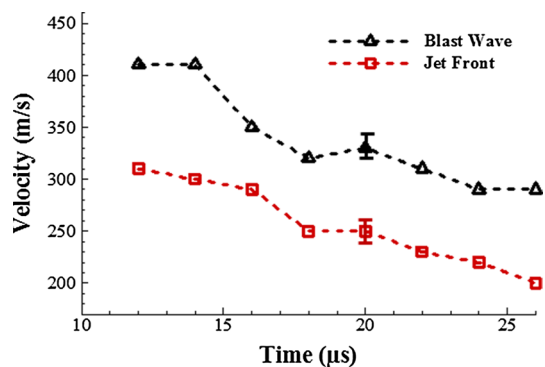


**Fig. 7** Blast wave and jet front propagation velocities at atmospheric conditions

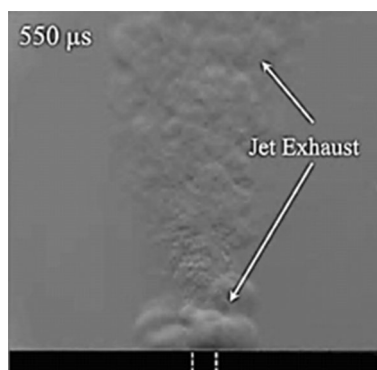


**Fig. 8** 550  $\mu\text{s}$  time delayed schlieren image of the flowfield created by the actuator in atmospheric conditions

Fig. 7. The maximum jet front and blast wave velocities were measured to be 310 m/s, about 12  $\mu\text{s}$  after the initial discharge and 410 m/s, approximately 14  $\mu\text{s}$  after the initial discharge, respectively. As seen in the plots, the velocities of the jet front and blast wave decay as the time increases from the initial SparkJet arc discharge. The increase in jet front and blast wave velocities that occurs approximately 20  $\mu\text{s}$  after the SparkJet is discharged has also been shown in previous studies (Foster et al. 2011) and is thought to be caused by the interaction of the initial and secondary blast waves.

The exhaust jet created by the single-orifice SparkJet actuator at a much larger time delay of 550  $\mu\text{s}$  is shown in Fig. 8. The jet created by the electrical discharge and initial heat generation inside of the cavity is still being sustained at these later time delays, and benchtop studies have revealed that the presence of the flow from the SparkJet can be seen up to 2 ms after the initial discharge. Previous analytical and experimental results have indicated that the pressure in the cavity of the actuator has settled to atmospheric pressure roughly 200  $\mu\text{s}$  after the initial discharge

(Haack et al. 2010). The features observed 550  $\mu\text{s}$  after the initial discharge may be primarily related to the thermal plume created by the intense electrical breakdown and unrelated to the high-momentum jet flow created by the actuator. Regardless, these results pose a possible limit on the maximum frequency that these actuators can be operated at while delivering maximum momentum throughput without an external air supply.

#### 4.1.2 400- $\mu\text{m}$ orifice array; atmospheric conditions

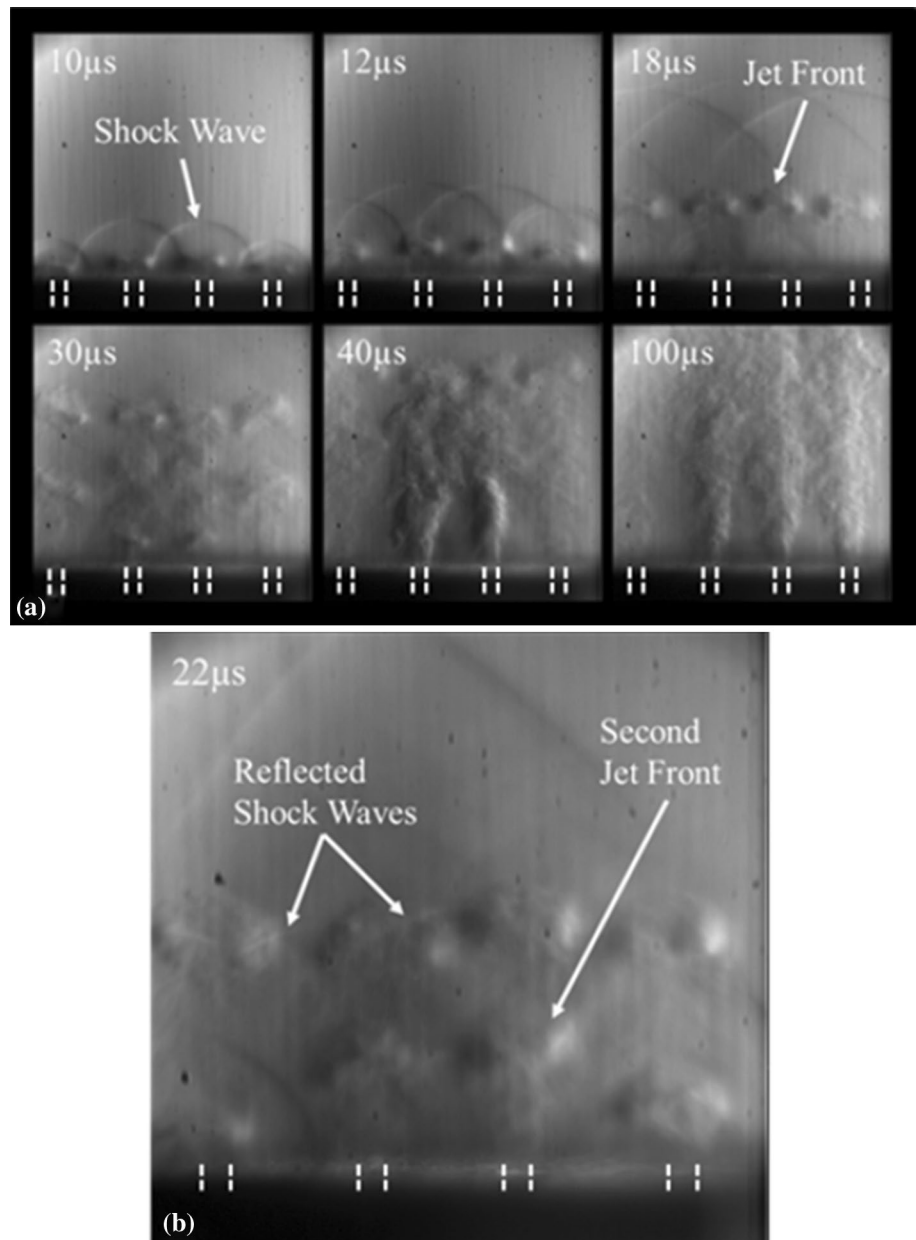
Schlieren images from previous studies of a four orifice externally triggered SparkJet array operating at atmospheric conditions are shown in Fig. 9 (Foster et al. 2011). It is interesting to observe the principal features found in Fig. 6 for the single-orifice actuator: An initial blast wave followed by a jet front are also observed in the flow visualizations of jets produced by an array of orifices. However, additional significant features are also present; these include multiple reflected blast waves and a second jet front. These features, seen in Fig. 9b approximately 22  $\mu\text{s}$  after the SparkJet is discharged, are labeled. The cause of the secondary jet front and blast waves is suspected to be due to the reflection of the initial blast wave within the cavity, which also produces a concomitant jet front, similar to the jet front that follows the initial blast wave.

An examination of the overall images at time delays of 18, 22, 30, and 40  $\mu\text{s}$  reveals that the four jets in the array have propagated nearly the same distance away from the actuator. However, the spherical blast waves of the two outside jets at time delays of 10 and 12  $\mu\text{s}$  have not propagated as far away from the actuator as the blast waves of the two center jets. The reason becomes apparent when one considers the fact that the electrodes, hence the spark, are located in the center of the actuator cavity. Since the two center orifices are closest to the spark and the disturbance it creates, i.e., the blast wave followed by the jet, the flow thus generated will emanate first from the center orifices. Another interesting flow feature is revealed at a time delay of 40  $\mu\text{s}$  and consists of a large density gradient across the two center jets in the array. This effect may be caused by the presence of high temperature exhaust gases which are mainly issuing through the center orifices. In summary, even though some end effects are observed, the flow produced by the array is reasonably uniform and similar to that produced from a single orifice.

The typical features observed in the operation of a SparkJet, a leading blast wave, followed by a jet whose front is a starting vortex is also very similar to impulsively started jets such as those produced from shock tubes (Arakeri et al. 2004). This is expected as the physical mechanism that produces both flows – an impulsive, high pressure source, are very similar. However, given the difference



**Fig. 9** Time delayed schlieren images of the exhaust from an externally triggered SparkJet at atmospheric conditions, **a** 10–100  $\mu\text{s}$  time delays, **b** 22  $\mu\text{s}$  time delay showing reflected shocks and second jet front (from Foster et al. 2011)



in scales between the current, ‘microscale’ flow (produced from 400- $\mu\text{m}$  orifices) and those studied from conventional, larger, lab-scale flows, the similarity in the principal feature is noteworthy if not remarkable.

#### 4.1.3 400- $\mu\text{m}$ orifice array; subatmospheric conditions

Time delayed schlieren images were also acquired of a four orifice externally triggered SparkJet array operating at a pressure of 60 kPa in a custom built vacuum chamber. This allowed for the actuator to be tested at pressures similar to those encountered during wind tunnel testing and at high-altitude flight conditions. It also allowed for a direct comparison of the actuator properties when operating in

atmospheric conditions. The SparkJet array was visualized at increasing time delays starting at a delay of 6  $\mu\text{s}$ , which is when the blast wave generated by the arc discharge is first seen exiting from the orifice array. Flowfield images were captured up to a delay of 70  $\mu\text{s}$ . As before, the four microorifices are marked by the white dashed lines in all of the images and a 5 mm reference scale is provided. Instantaneous images from several of these time delays are shown in Fig. 10.

Results of the subatmospheric testing of the four-orifice actuator array reveal flow features similar to those observed at atmospheric conditions including an initial blast wave and jet front. The presence of multiple blast waves is also seen in both atmospheric and subatmospheric testing. A

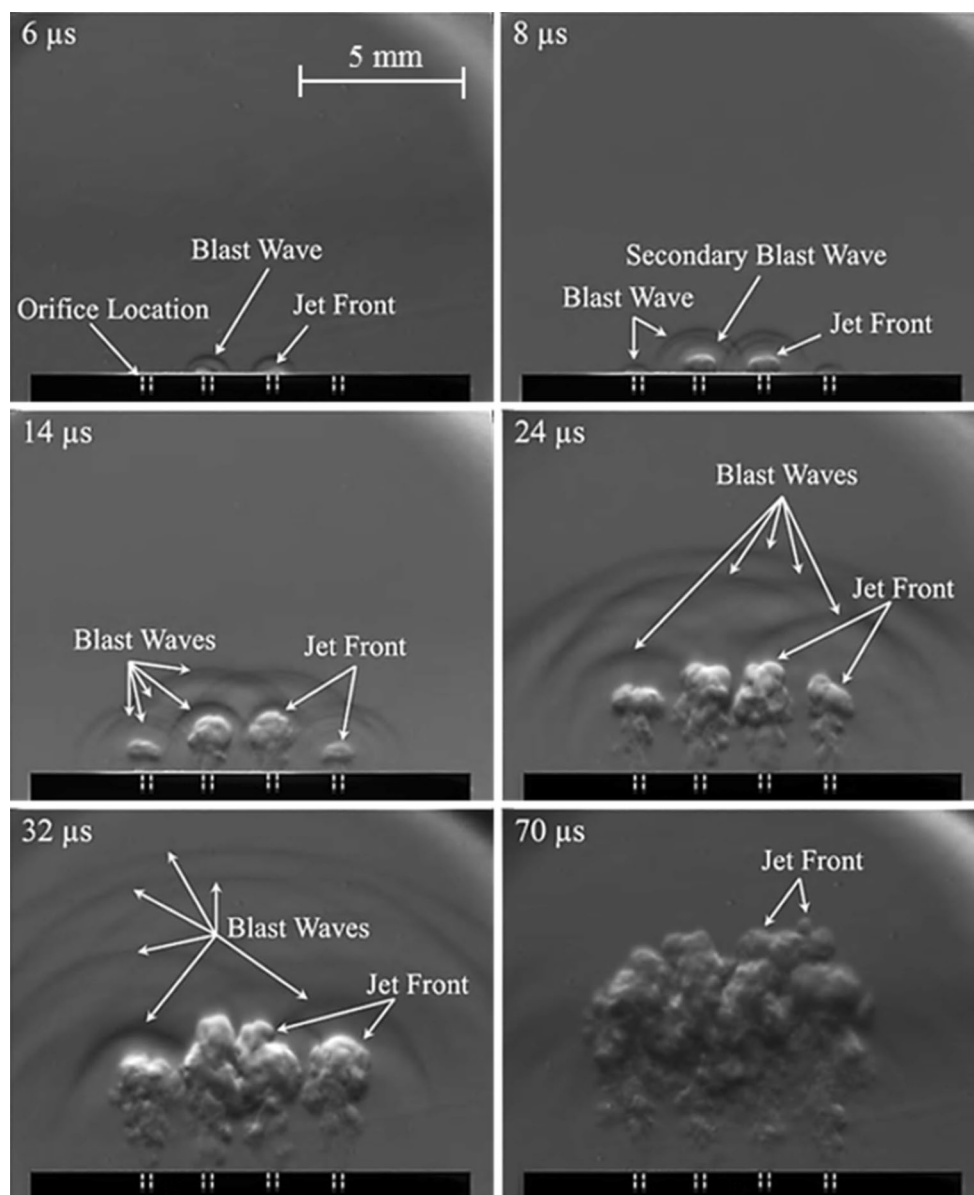


**Fig. 10** Time delayed schlieren images of the exhaust from an externally triggered four orifice SparkJet operating at 60 kPa

secondary blast wave can be seen in the image corresponding to a time delay of  $8 \mu\text{s}$  similar to the secondary blast wave seen in the single-orifice SparkJet tested at atmospheric conditions. Again, the difference in the sources of the initial blast wave and secondary blast wave is not entirely clear. The occurrence of multiple blast waves seen in the images is believed to be due to reflections of the original blast wave in the cavity. Furthermore, the high density gradient of the two center jets is not present at a time delay of  $40 \mu\text{s}$  in subatmospheric conditions as was seen in atmospheric conditions (see Fig. 9). Also, the four jets in the array do not propagate at roughly the same velocity as was observed at atmospheric conditions. The two center

jets travel a longer distance from the actuator than the two outside jets during subatmospheric testing, this is readily visible in the images corresponding to time delays up to  $24 \mu\text{s}$ . While the blast waves and jet fronts are first seen exiting the two center orifices during atmospheric testing at early time delays ( $t < 12 \mu\text{s}$ , see Fig. 9), this feature is more clearly visible during subatmospheric testing for  $t < 14 \mu\text{s}$ . This is in part because the difference in the jet and blast wave propagations between orifices is most visible at early time delays, and only two early time delays were obtained for atmospheric tests ( $t = 10$  and  $12 \mu\text{s}$ ). As explained in Sect. 4.1.2, the reason the features are first seen exiting the center orifices is because the spark is centered in the

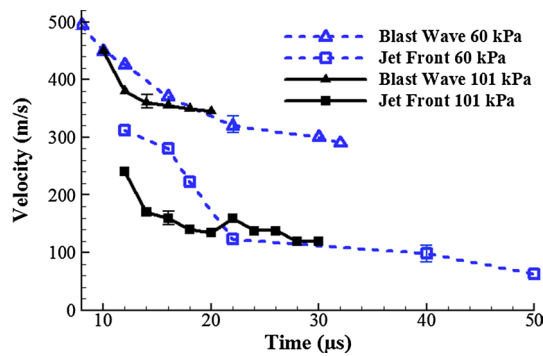


**Fig. 11** Blast wave and jet front velocity estimates

cavity of the actuator and therefore the two center orifices are closest to the spark. The propagation speeds of the jet fronts become more uniform as the flow evolves further, being roughly equal at a time delay of 70  $\mu\text{s}$  and onwards after the SparkJet discharge.

The propagation speeds of the initial blast wave and jet front were estimated from these time-resolved visualizations at atmospheric and subatmospheric conditions and are shown in Fig. 11. For both the atmospheric and subatmospheric cases, the initial blast wave is followed by a jet front which propagates at a slower velocity than the blast wave. As expected, the blast wave and jet front velocities decay as they travel away from the actuator under the two different ambient conditions. The velocities of the blast wave at atmospheric and subatmospheric conditions at a time delay of 10  $\mu\text{s}$  were both found to be 450 m/s. The jet front velocities at atmospheric and subatmospheric conditions at a time delay of 12  $\mu\text{s}$  were found to be 240 and 310 m/s, respectively. These results indicate that the potential control authority of the SparkJet may increase at lower ambient pressures encountered in tunnel tests and/or flight conditions at high altitudes due to the increased jet front velocity. However, a lower ambient pressure may also result in a lower density jet created by the SparkJet and may potentially counteract the benefit of an increase in jet velocity. The mass flux ( $\rho V$ ) of the flow produced by the SJ was not measured in this study. It is a very difficult, near impossible, to make measurement with current methods given the very high speeds, small scales, and temperatures associated with this flow.

#### 4.1.4 Effect of trigger mechanism on actuator flowfield at atmospheric conditions

The blast wave and jet front propagation speeds of a four-orifice SparkJet actuator employing an external trigger were compared to a similar actuator that utilized a pseudo-series trigger, as seen in Fig. 2. The results are shown in Fig. 12. The average velocity of the blast wave created by

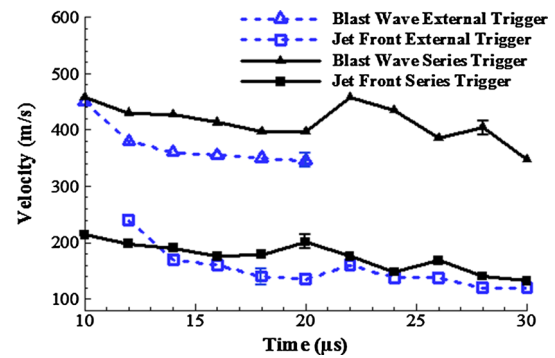


**Fig. 12** Blast wave and jet front velocity calculations for an external and pseudo-series trigger mechanism

the actuator employing the pseudo-series trigger is roughly 60 m/s greater, for time delays between 12 and 20  $\mu\text{s}$ , than the blast wave generated by the actuator employing an external trigger. The jet front velocity of the actuator that incorporates a pseudo-series trigger is also nominally higher for most of its lifetime, when compared to the actuator that employs an external trigger. While the velocity differences are not drastic, the findings do support that using a pseudo-series trigger mechanism increases the efficiency of the actuator (please see Popkin et al. 2013 for details).

#### 4.1.5 Effect of orifice diameter on actuator flowfield at atmospheric conditions

Instantaneous phase-conditioned schlieren images of a pseudo-series triggered actuator comprised of an array of four 800- $\mu\text{m}$  orifices operating at atmospheric conditions can be seen in Fig. 13. As before, the orifices have been marked by white dashed lines and a 5 mm reference is shown for scaling purposes. A comparison to the images in Figs. 9 and 10 confirms that the flowfield contains similar features as those seen before, comprising of jet fronts and multiple blast waves. The exhaust created by the actuator is clearly seen even 750  $\mu\text{s}$  after the discharge is initiated. To quantify the effect of orifice size, the velocities of the jet fronts and blast waves created by a four orifice actuator with 400- $\mu\text{m}$ -diameter orifices and an actuator with 800- $\mu\text{m}$ -diameter orifices are shown in Fig. 14. The actuators both utilize pseudo-series triggers and have the same actuator cavity volume. As expected, based on conservation of mass, the velocity features generated by the actuator with 400- $\mu\text{m}$ -diameter orifices are higher than those generated by the 800- $\mu\text{m}$ -diameter actuator. At a time delay of 10  $\mu\text{s}$ , the blast wave from the 400- $\mu\text{m}$  orifice actuator is roughly 25 m/s greater than the blast wave created by the 800- $\mu\text{m}$  actuator. The difference in blast wave propagation increases dramatically, as much as 100 m/s at later times. The difference in the jet propagation velocity is similar,

**Fig. 13** Time delayed schlieren images of the exhaust from an 800- $\mu\text{m}$  four orifice pseudo-series triggered SparkJet

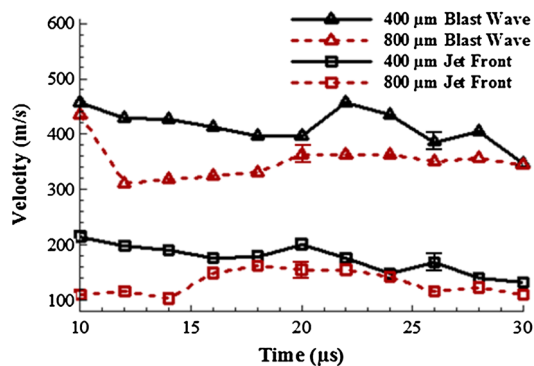
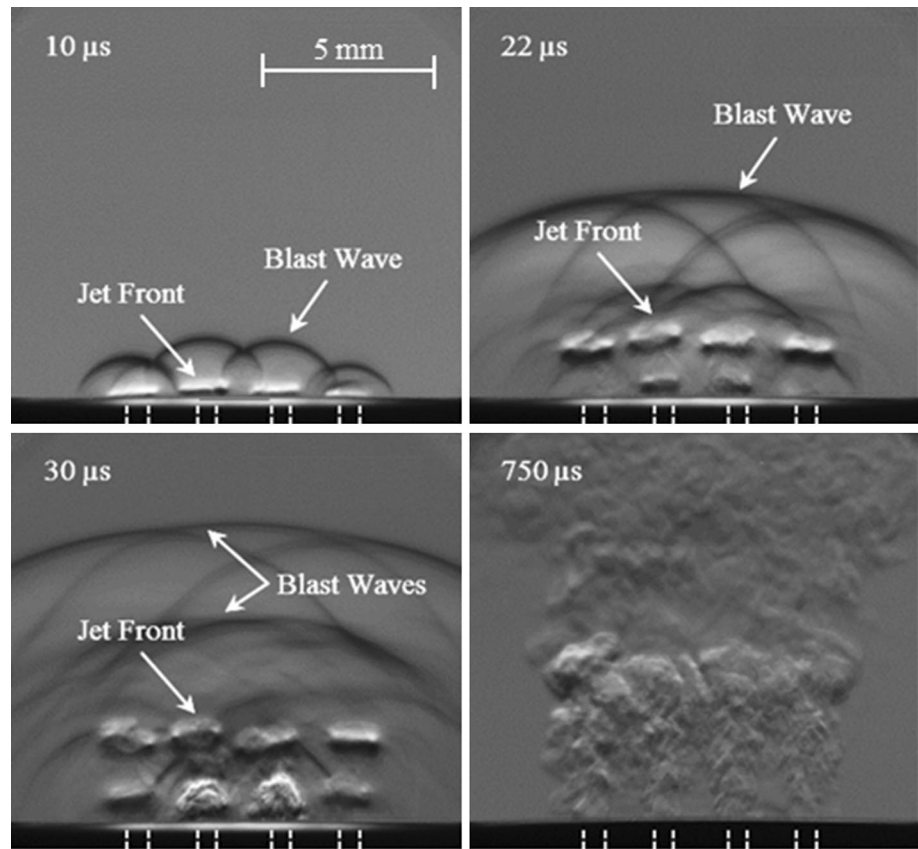


**Fig. 14** Comparison of the effect of orifice diameter on jet front and blast wave velocities

where the jet front generated by the 400- $\mu\text{m}$  actuator propagates much faster, by as much as 100 m/s greater in the early stages of the flow evolution,  $t < 15 \mu\text{s}$ .

#### 4.2 Flow properties under burst mode operation

The dominant frequencies associated with the instabilities in most high-speed flowfields are on the order of a kilohertz and above. For an actuator to effectively excite these instabilities, it must be able to operate at these high

frequencies. The SparkJet actuator utilizes a burst mode firing sequence to operate up to a kilohertz for a fixed number of discharges. Following the single-shot tests previously discussed, schlieren images of two SparkJet actuator arrays were acquired, while the actuators were operating in burst mode on the benchtop. The two actuators tested utilize a pseudo-series trigger mechanism and have four orifices, the first having 400- $\mu\text{m}$ -diameter orifices and the second having 800- $\mu\text{m}$ -diameter orifices.

The cavity of the actuator was supplied with air at various supply pressures during the burst mode operation on the benchtop. An external cavity air supply was introduced to determine if it could aid in the refresh time of the actuator. The effects of various refill/refresh supply rates, denoted by the refill supply pressures were also examined. The following discussion will be limited to the 400- $\mu\text{m}$  actuator with refill supplies of 0 (no supply), 9.7 and 20 kPa. It should be noted that the pressures quoted here are measured at the source of the supply, and the actual total pressures of the supply inside the cavity is expected to be much lower due to the very small tube and orifices through which the refill air is connected. Thus, the actual pressure inside the cavity could not be accurately measured. Time delays of 20, 22, and 24  $\mu\text{s}$  were used for image acquisition during the burst mode tests where actuator discharge or burst frequencies of 500, 700, and 1,000 Hz were investigated.

Results from the 400- $\mu\text{m}$  orifice array actuator operating at frequencies of 500 and 1,000 Hz at a time delay of 24  $\mu\text{s}$  are presented below. The flow properties of the actuator at time delays of 20 and 22  $\mu\text{s}$  and at a frequency of 700 Hz are similar to those presented below and are not discussed to avoid repetition.

#### 4.2.1 400- $\mu\text{m}$ array; 500 Hz; various refill supply pressures at atmospheric conditions

The phase-locked schlieren images shown in Fig. 15 compare the effect of different cavity refill supply pressures on the flowfield created by the four orifice, 400- $\mu\text{m}$  SparkJet actuator. The actuator operated in bursts of 11 discharges at a frequency of 500 Hz (between each pulse within a burst). The images capture the flowfield created by the 10th discharge in the firing sequence at a time delay of 24  $\mu\text{s}$  after the discharge initiation.

The familiar features of blast waves and jet fronts are present in all of the images. A new feature observed during burst mode operation testing is the presence of a thermal

plume. The thermal plume is created by the high-frequency repetition which leads to intense heating of the actuator components as well as the air inside the actuator cavity. These results suggest that the accumulation of thermal energy in the burst mode may have an appreciable impact on the actuator throughput, especially if the burst mode involves a large number of pulses and/or is discharged at very high frequencies. The distinction between the effects of the jet flow and the effects of the thermal plume on the ambient fluid will have to be better characterized and understood if such devices are to be reliably used for active flow control.

The schlieren images of the flowfield acquired when there is no cavity refill supply define a baseline case for comparisons and contrasts to be made to the flowfield created by the actuator when a cavity refill supply pressure is present. A refill supply pressure 9.7 kPa has a significant influence on the jet structure and its evolution. The distinct sets of mushroom-shaped vortical structures observed at the jet front without a refill are substantially altered and ‘diffused’ by the addition of a cavity refill supply pressure.

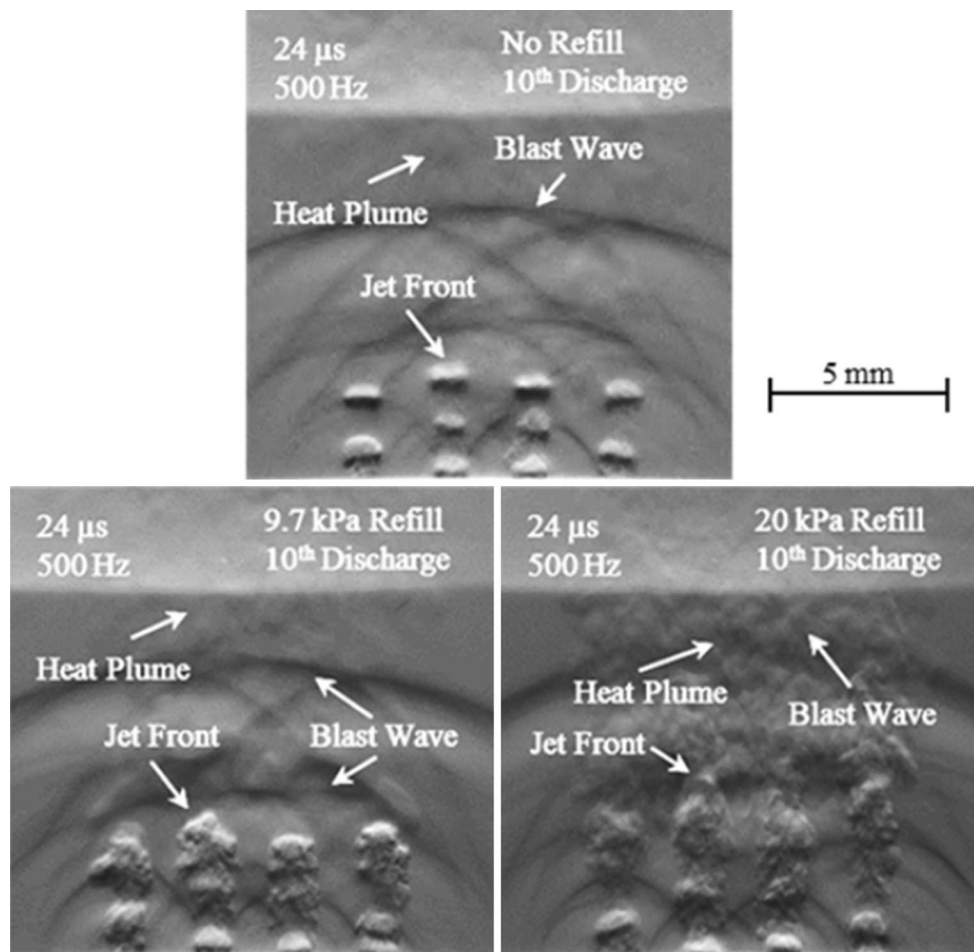


**Fig. 15** Burst mode operation of 400- $\mu\text{m}$  actuator array operating at 500 Hz with various cavity refill supply pressures

The presence of the cavity refill/supply air is seen being expelled from the orifices, this is more clearly evident for a supply pressure of 20 kPa. A comparison between the three cases in Fig. 15 reveals that the blast wave is visually weaker, especially when the supply pressure is 20 kPa. Furthermore, the thermal plume appears stronger, presumably because the refill air exhausting through the orifices is heated by the thermal mass accumulated in the actuator during operation.

#### 4.2.2 400- $\mu\text{m}$ array; 1 kHz; various refill supply pressures at atmospheric conditions

The 400- $\mu\text{m}$  orifice diameter SparkJet array was studied while operating in burst mode up to a frequency of 1 kHz. As before, the 10th discharge in the firing sequence is shown in Fig. 16 at a time delay of 24  $\mu\text{s}$ . The larger density gradient associated with the heat plume indicates that the intensity of the heat plume is increased in these images when compared to the images in Fig. 15 when the actuator

was operating at 500 Hz. The jet structures at this frequency for all air refill supply pressures do not contain the typical vortical mushroom/horseshoe structures seen in Fig. 15, i.e., the jet leading edge is much more diffused and turbulent compared to the 500 Hz case. There is little difference in the flow dynamics between the cases of no air refill supply and an air refill supply pressure of 9.7 kPa. Increasing the air refill supply pressure to 20 kPa intensifies the signature of the heat plume in the images. The blast waves are less distinct as the air refill supply pressure is increased and also less distinct when compared to burst mode operation at 500 Hz.

## 5 Wind tunnel studies

The SparkJet array was installed in the wind tunnel and was first operated under no-flow or quiescent conditions. Phase-conditioned shadowgraph images of the SparkJet array flowfield were acquired to confirm reliable operation

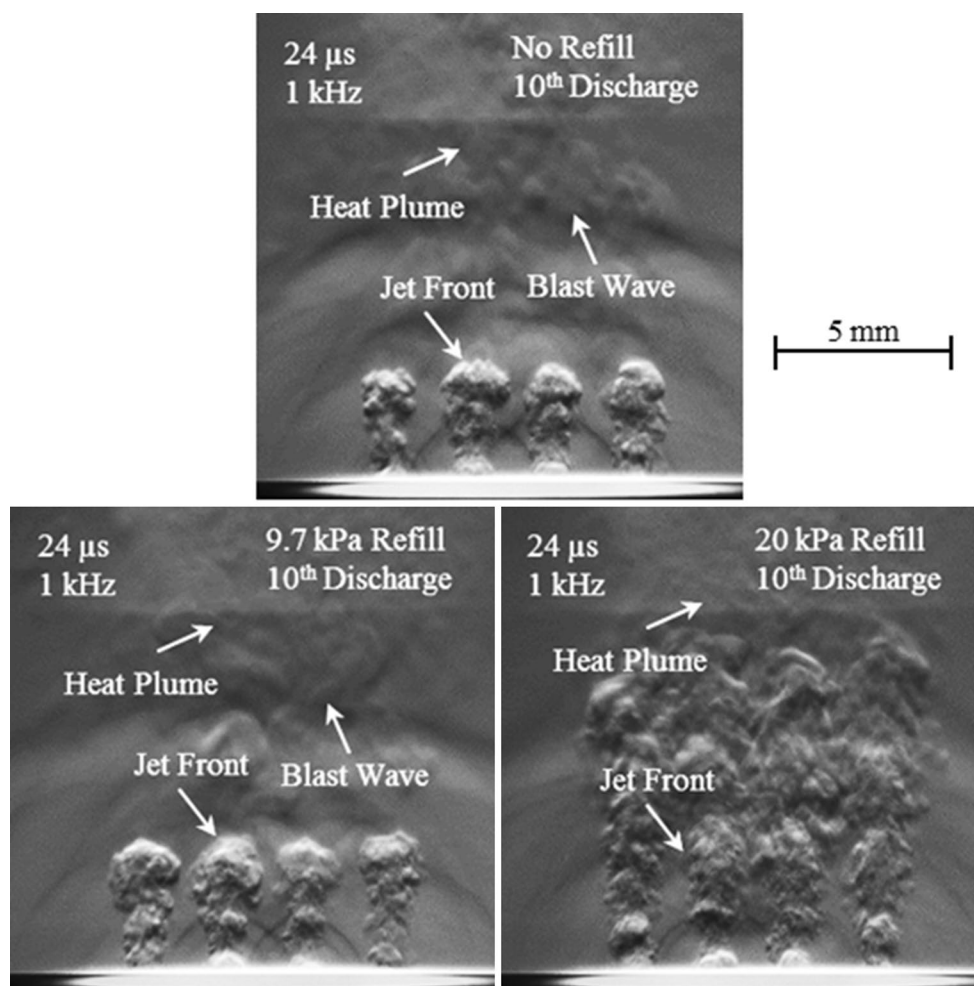


**Fig. 16** Burst mode operation of 400- $\mu\text{m}$  actuator array at 1 kHz with various cavity refill supply pressures

of the device and to visualize the actuator flow in the single-shot and burst operating modes of the actuator. These quiescent flow tests were followed by supersonic flow tests beginning with baseline shadowgraph images where the SparkJet array was not active. Finally, phase-conditioned shadowgraph images of the SparkJet array operating in the single-shot and burst modes in a Mach 1.5 crossflow were acquired. As mentioned in Sect. 2, the microarray is oriented normal to the incoming Mach 1.5 crossflow.

### 5.1 Quiescent flow results at atmospheric conditions

The phase-conditioned shadowgraph images shown in Fig. 17 are of the SparkJet operating in single-shot mode with no tunnel flow. The entire 76 mm height ( $h = 76$  mm) of the test section is visualized in these images. Since the shadowgraph technique provides an integrated image over the entire optical path of the light, these images show the SparkJet array such that the flowfield from all twelve jets is visible along this optical path; the array location is marked by the white dashed lines in all images.

Features seen in the benchtop experiments are also seen here. Multiple blast waves, as well as the jet exhaust, can be seen in all of the images. The image at a time delay of  $100 \mu\text{s}$  reveals that the jet front has propagated roughly 5 mm away from the actuator, while the extent of the

furthest blast wave is roughly at the center of the test section (38 mm). The average velocity of the blast wave and jet front, measured from the initial discharge to  $100 \mu\text{s}$  after the initial discharge, are 430 and 87 m/s, respectively. Although quantitative data at such large time delays was not acquired in benchtop experiments discussed in Sect. 4.1.4, these values correlate well over the time delays (up to  $30 \mu\text{s}$ ) that velocity values were found for the  $400 \mu\text{m}$  externally triggered SparkJet array during the benchtop testing of the actuators. Comparisons between the benchtop velocity estimates and quiescent wind tunnel velocity estimates reveal that the jet front loses momentum more quickly than the blast wave in both cases. The trend of the blast waves propagating at a much greater velocity than the jet front continues in these images, and the blast waves can be seen to travel completely across the test section at a time delay of  $200 \mu\text{s}$ .

The shadowgraph images shown in Fig. 18 correspond to the quiescent flow tests in *burst mode* with the SparkJet being discharged 40 times at a rate of 700 Hz. The first image in Fig. 18 shows the first discharge in the burst mode at a time delay of  $100 \mu\text{s}$  and reveals essentially the same flow features as the corresponding single-shot mode image in Fig. 17. As the SparkJet array continues to discharge in the burst mode, a noticeable thermal plume appears and propagates away from the SparkJet array orifices as seen in the images of subsequent shots—10 and 40, at time delays of  $100 \mu\text{s}$ . The last image reveals that the thermal plume exists after the SparkJet has stopped discharging as evident by the lack of blast waves and presence of a heat plume. These results support the observations in benchtop experiments in burst mode (see Figs. 15 and 16), confirming that the accumulation of thermal energy in the burst mode may have an appreciable impact on the actuator throughput, especially if the burst mode involves a large number of pulses.

### 5.2 Baseline, SparkJet actuator off

A shadowgraph image of the baseline freestream flow was acquired prior to actuator operation and is shown in Fig. 19. The direction of the flow is from left to right, and the field of view spans the 76 mm height of the test section. The Mach waves seen in the image are oriented at approximately  $43^\circ$ , corresponding to  $M_\infty \sim 1.5$ . The first Mach wave is due to a surface joint between the nozzle block and the test section, and the second is due to the presence of the actuator orifices. The spots on the image are due to contaminants associated with the mirrors and camera lens. In subsequent results, the oblique shock generated by the SparkJet is compared to the baseline image and allows for an estimate to be made of the flow turning angle due to SparkJet operation.

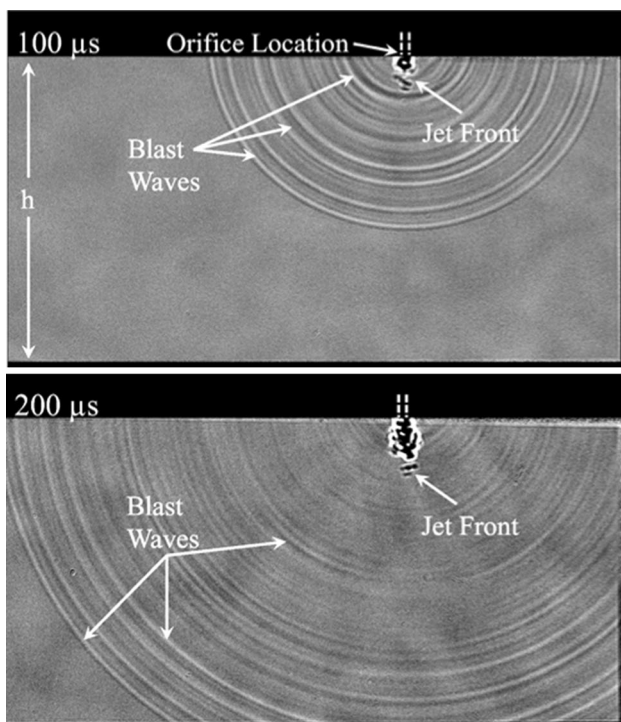


**Fig. 17** Shadowgraph images of the SparkJet array installed in the wind tunnel operating in single-shot mode with no freestream flow in the test section. ( $h$  Height of test section)

**Fig. 18** Instantaneous shadowgraph images of the SparkJet array installed in the wind tunnel operating in *burst mode* with no freestream flow in the test section

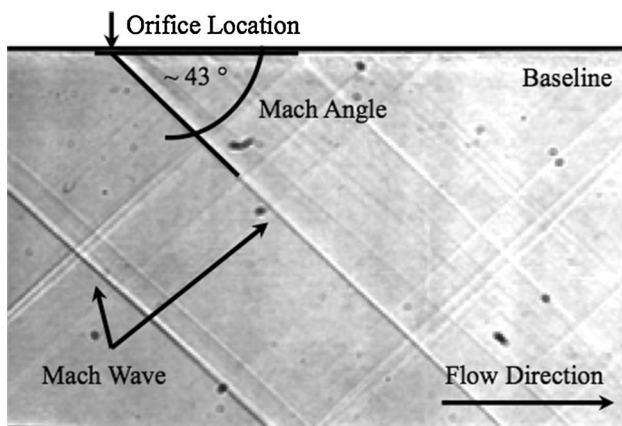
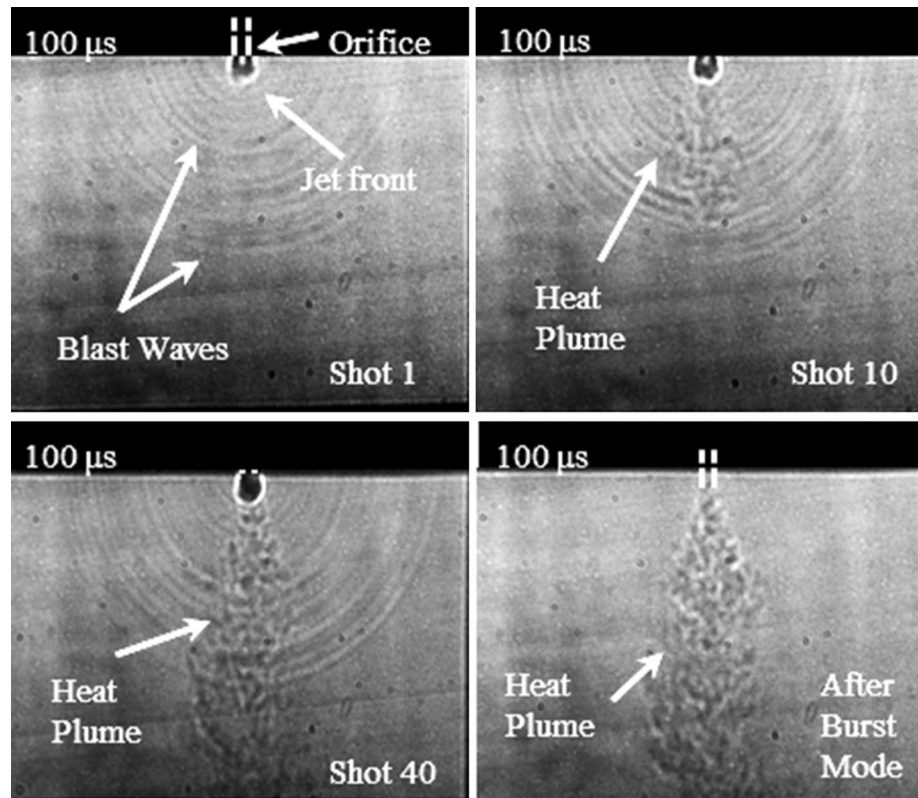


**Fig. 19** Baseline, no actuator flow, shadowgraph image of the test section

### 5.3 Flow properties in supersonic crossflow

#### 5.3.1 Single-shot mode

The SparkJet actuator was subsequently operated in single-shot mode in a Mach 1.5 crossflow. As before, the shadowgraph images shown in Fig. 20 were taken with increasing time delays between the light source trigger and the SparkJet discharge. These images span the entire height (76 mm) of the test section and show the Mach wave due to the surface

joint and also clearly reveal the formation of a stronger wave, an oblique shock, originating at the SparkJet orifice and being followed by an expansion fan. These features have been marked in Fig. 20. The images also show that the oblique shock develops and propagates across the test section with increasing time delays. The images corresponding to time delays between 75 and 225  $\mu\text{s}$  reveal the presence of blast waves downstream of the oblique shock in the expansion fan, these blast waves steadily propagate away from the SparkJet orifices. As the blast waves move away from the orifices, the oblique shock wave is ‘pushed’ slightly, where this is seen as a kink or bulge in the shock wave. This feature also propagates concomitantly with the blast waves as the flow develops due to SparkJet actuation. The spots on the images are due to contaminants associated with the mirrors and camera lens.

Comparisons between the images in Fig. 17, taken with no tunnel flow, and those shown herein reveal that the blast waves created by the actuator may have a stronger, or at least a comparable, effect on the flowfield relative to the jets produced by the SparkJet. The oblique shock generated by the actuator follows the blast waves and propagates across the test section at a rate greater than the jet front. The effect of the jet front may sustain the oblique shock and provide the momentum throughput to maximize the oblique shock angle.

The oblique shock angle evolution as a function of time is shown in Fig. 21. The maximum oblique shock angle of



**Fig. 20** Shadowgraph images of the SparkJet array (single-shot mode) in Mach 1.5 flow at various time delays

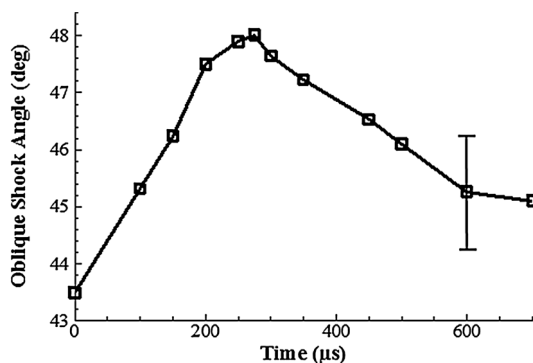
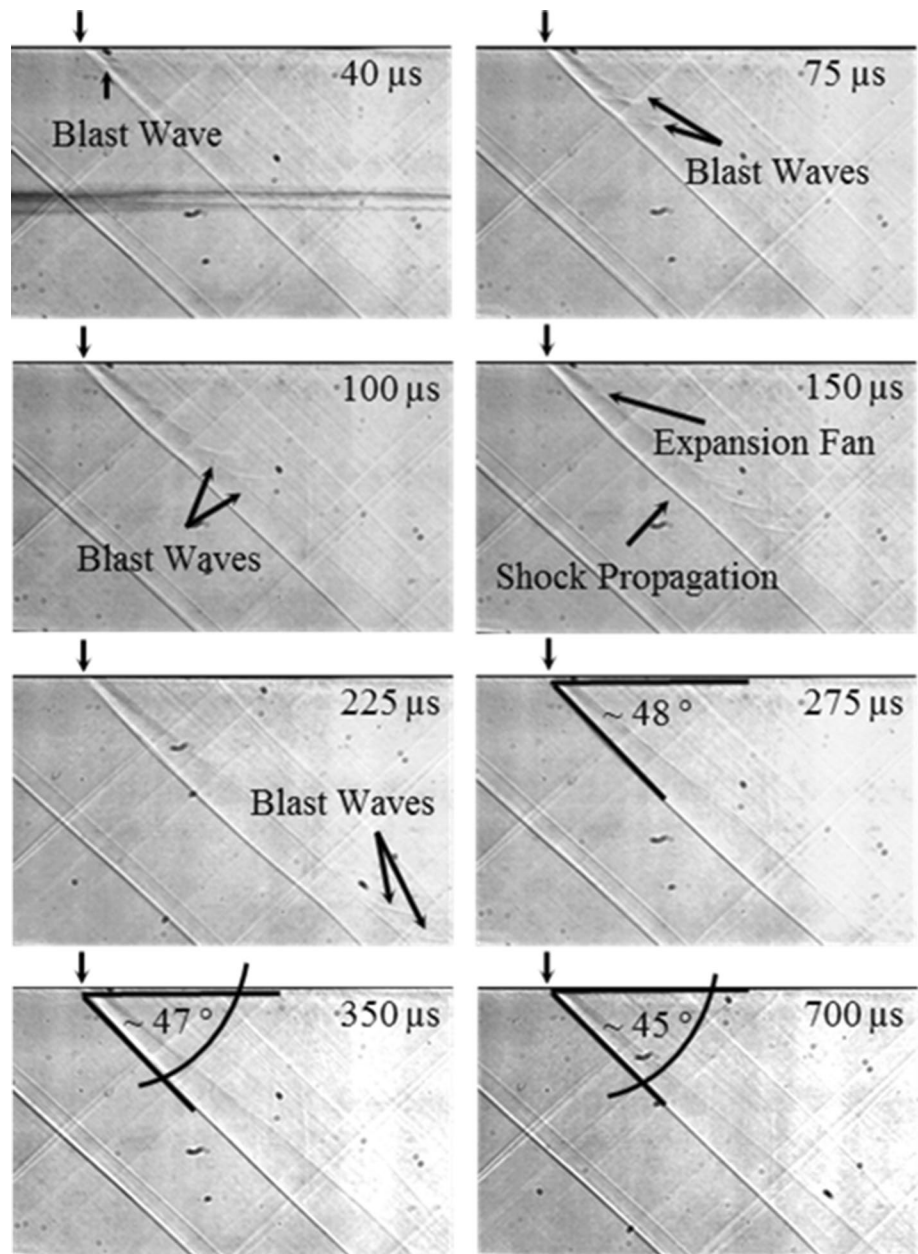
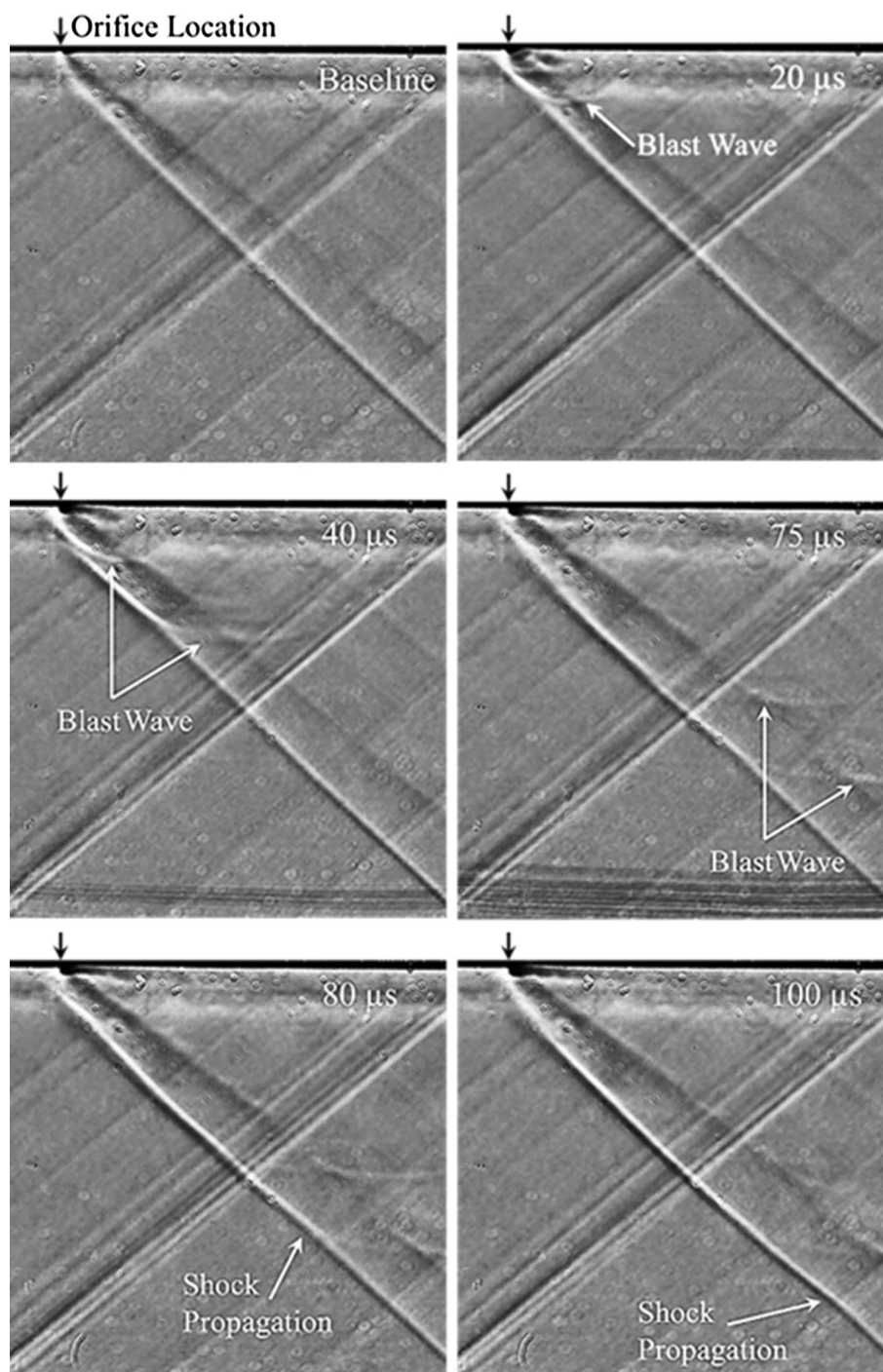


**Fig. 21** Oblique shock angle evolution

approximately  $48^\circ$ , which is equivalent to a  $5^\circ$  flow turning angle, occurs  $275 \mu\text{s}$  after the SparkJet is discharged. The image corresponding to a time delay of  $350 \mu\text{s}$  shows that the oblique shock has propagated across the entire length of the test section and has a measured angle of  $47^\circ$ . The oblique shock angle is approximately  $46^\circ$  at a time delay of  $500 \mu\text{s}$  and at an angle of  $45^\circ$ ,  $700 \mu\text{s}$  after the discharge revealing that the flow is relaxing back to freestream conditions. It is assumed that the shock wave will asymptotically return to a Mach wave at extended time delays.

Phase-locked shadowgraph images of the actuator influencing the Mach 1.5 flowfield were also taken over a smaller field of view to visualize the flowfield in greater detail. Shorter

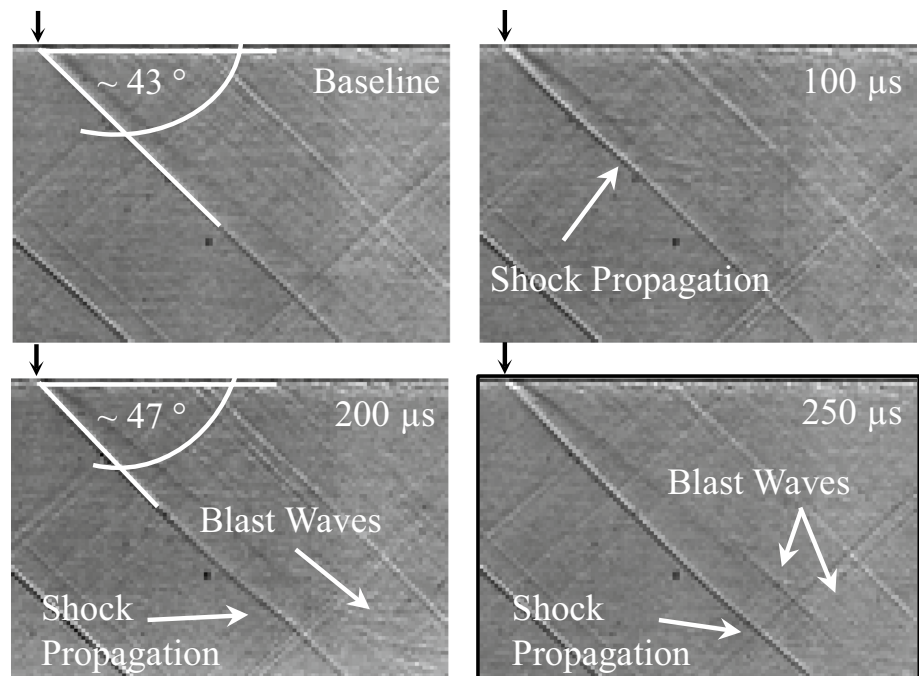
**Fig. 22** Shadowgraph images showing boundary layer interaction in Mach 1.5 flow



time delays were used in order to examine the early evolution of the flow from 0 to 100  $\mu\text{s}$ . The resulting shadowgraph images can be seen in Fig. 22. The blast waves created by the SparkJet actuator are first seen 20  $\mu\text{s}$  after the initial discharge. The blast waves can also be seen interacting with the tunnel boundary layer at these short time delays. The blast waves are observed to be propagating away from the tunnel ceiling with increasing time delays. As observed in the global flow-field images in Fig. 20, the oblique shock generated by the

actuator tracks the blast waves and the kink or bulge in the oblique shock has nearly propagated across the entire field of view by 100  $\mu\text{s}$ . The shadowgraph images shown in Figs. 20 and 22 confirm the SparkJet actuator's control authority in the supersonic flow and allow for a direct comparison to be made between the influence of the pulsed SparkJet actuator to the previously studied steady microjet injection in supersonic crossflow (Kumar et al. 2011). This comparison is made later in Sect. 5.4.

**Fig. 23** Instantaneous shadowgraph images corresponding to the 40th discharge, at various time delays, during *burst mode* operation



### 5.3.2 Burst mode

The SparkJet was operated in burst mode and discharged 40 times at a frequency of 700 Hz to study and compare its effectiveness to the single-shot operating mode. Instantaneous shadowgraph images of the 40th discharge in burst mode are shown in Fig. 23. The burst mode operation of the actuator creates similar flow features to those seen in the single-shot operating mode. As before, each image spans the entire height (76 mm) of the test section. Blast waves can be seen in the images corresponding to 100, 200, and 250  $\mu\text{s}$  time delays. The blast waves are followed by an oblique shock that is ‘pushed’ slightly forming a kink or bulge that propagates across the test section with increasing time delay.

A plot of the oblique shock angle evolution created by the first and last discharges in the operating sequence can be seen in Fig. 24. The graph shows that the strength of the oblique shock angle created by the last discharge of the operating sequence is very similar to the first in the sequence. The momentum throughput from the first discharge is almost identical to the 40th discharge indicating that the refresh cycle is completed by the time the next discharge occurs. Oblique shock angle measurements reveal that at a time delay of 200  $\mu\text{s}$ , the 40th discharge of the actuator generates a  $47.2^\circ$  oblique shock. This oblique shock angle is the same angle generated by the first discharge in burst mode at the same time delay. The nearly identical shock angles at earlier time delays, 100 and 200  $\mu\text{s}$ , reveal that there is no measurable loss in actuator efficacy in terms of its impact on Mach 1.5 flow

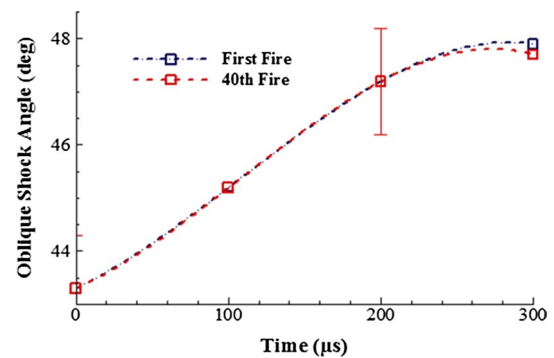


**Fig. 24** Oblique shock angle evolution comparing first and last discharge of actuator in burst mode

at a discharge frequency of 700 Hz. We suspect that similar efficacy in terms of control authority may be obtained at higher repetition rates; however, we were unable to test this due to challenges associated with the actuator power electronics.

### 5.4 Comparison to steady microjets

Here, we very briefly compare the effect of the SparkJet array to the previously reported work (Kumar et al. 2011) involving steady microjets in the same wind tunnel facility under similar conditions. A plot of the oblique shock angle created by steady microjets at various Microjet Pressure Ratios (MPR) and also of the oblique shock angle created by the SparkJet is shown in Fig. 25. MPR is defined as the ratio of microjet supply total pressure to the tunnel

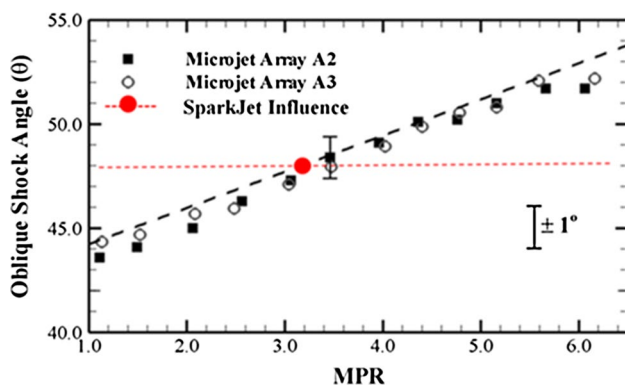


**Fig. 25** Oblique shock angle resulting from steady microjet array and from the SparkJet array

stagnation pressure. Arrays A2 and A3 were at different streamwise locations and, therefore, the boundary layer conditions were slightly different for each array. Figure 25 shows that the microjet array performance was not affected by the change in boundary layer conditions and, in fact, the effect of the microjet versus MPR is nearly linear. (Please see Kumar et al. 2011 for details.)

To compare the effect of steady microjets with the unsteady SparkJet array, the maximum oblique shock angle of  $48^\circ$  is represented by the red dashed line and the intersection of this line with the linear approximation of the steady microjet performance is shown by the filled red circle. This comparison suggests that the maximum influence from the tested SparkJet array is nearly as effective as the steady microjets at an MPR (Microjet Pressure Ratio) of 3.2. It should be noted that the steady microjets cause a constant shift in the oblique shock angle, while the unsteady SparkJet creates a temporal shift ( $\sim 0.7$ – $1.0$  ms).

## 6 Conclusions

The control authority of the SparkJet actuator was characterized under various actuator design and operating parameters. SparkJet actuator designs employing a three-electrode external trigger and a two-electrode pseudo-series trigger mechanism were studied on the benchtop using a laser-based microschlieren technique. The actuator flowfield was characterized in a quiescent ambient environment at atmospheric and subatmospheric conditions. The fast response time of the actuator and the high-momentum blast waves and jet fronts present in the flowfield suggest the potential for requisite control authority for high-speed flow control. For a single-orifice SparkJet actuator, the maximum velocity of the blast waves was found to be 410 m/s, while the maximum jet front velocity was found to be 310 m/s at atmospheric conditions. Microschlieren benchtop results of a four-orifice SparkJet actuator

array operating in atmospheric and subatmospheric conditions revealed jet front velocities measuring 240 and 310 m/s, respectively. The highest velocities, leading to a higher control authority, were obtained at subatmospheric pressures encountered in high-altitude flight conditions.

The interaction of a SparkJet array with a Mach 1.5 cross-flow was visualized using high-resolution shadowgraphy. Time-resolved shadowgraph images confirmed the actuators control authority in supersonic flow by revealing a maximum flow turning angle of  $5^\circ$  roughly 275  $\mu$ s after the SparkJet actuator was triggered in a single-shot operating mode. Similar results were obtained when the actuator was operated in burst mode at 700 Hz. The maximum turning angle generated is equivalent to that created by a steady microjet at a microjet pressure ratio of 3.2. The agreement between the single-shot and burst mode operation and the actuator's ability to significantly impact the external supersonic flow demonstrates its potential for high-speed flow control, especially when fast actuation and/or high repetition rates are needed.

However, as is the case with almost any actuator—there is no silver bullet, some challenges exist. These are primarily associated with the actuator power electronics and material (see Popkin et al. 2013 for details) and need to be addressed. Our results also show that actuator performance may also be impacted in burst operation due to thermal management issues. Future designs need to address some of these issues. If addressed, the resulting improved SparkJet actuator shows potential as an effective actuator with some unique properties for control of high-speed flows. One such improvement is the change from a three-electrode actuator to a two electrode design, which has resulted in a theoretical operating efficiency increase from 30 to 75 % (Popkin et al. 2013). The two electrode design allows for a pseudo-series trigger mechanism and a larger electrode gap distance which was characterized on the benchtop using a laser-based microschlieren system. Similar to present work, detailed studies of future, improved SparkJet designs, which examine the actuator's performance and impact upon representative supersonic/hypersonic flows, are needed.

**Acknowledgments** The authors would like to thank Dr. Jonas Gustavson, Nishul Arora, and Phil Kreth for their guidance and helpfulness and also Bobby Avant and Adam Piotrowski for their machining expertise. Lastly, thank you to the Florida Center for Advanced Aero-Propulsion at Florida State University and the Air Force Office of Scientific Research for their support.

## References

- Ali MY, Solomon JT, Gustavsson J, Kumar R, Alvi FS (2010) Control of resonant flow inside a supersonic cavity using high bandwidth pulsed micro-actuators. 48th AIAA Aerospace Sciences Meeting Including the New Horizons Forum and Aerospace Exposition. doi:10.2514/6.2010-1198

- Ali MY, Alvi FS, Kumar R, Manisankar C, Verma SB, Venkatakrishnan L (2013) Studies on the influence of steady microactuators on shock-wave/boundary-layer interaction. *AIAA J* 51(12):2753–2762
- Alvi FS, Lou H, Shih C, Kumar R (2008) Experimental study of physical mechanisms in the control of supersonic impinging jets using microjets. *J Fluid Mech* 613:55–83
- Arakeri JH, Das D, Krothapalli A, Lourenco L (2004) Vortex ring formation at the open end of a shock tube: a particle image velocimetry study. *Phys Fluids* 16:1008
- Caruana D, Rogier F, Dufour G, Gleyzes C (2013) The plasma synthetic jet actuator, physics, modeling and flow control application on separation. *Aerosp Lab J AL06-10:1–13*
- Diez-Garias FJ, Dahm WJA, Paul PH (2000) Microactuator arrays for sublayer control in turbulent boundary layers using the electrokinetic principle. 38th Aerospace Sciences Meeting & Exhibit. doi:[10.2514/6.2000-548](https://doi.org/10.2514/6.2000-548)
- Fernandez E, Kumar R, Alvi F (2013) Separation control on a low-pressure turbine blade using microjets. *J Propuls Power* 29(4):867–881. doi:[10.2514/1.B34413](https://doi.org/10.2514/1.B34413)
- Foster CH, Solomon JT, Alvi FS (2011) Visual study of resonance dominated microjet flows using laser-based micro-schlieren. 49th AIAA Aerospace Sciences Meeting including the New Horizons Forum and Aerospace Exposition. doi:[10.2514/6.2011-766](https://doi.org/10.2514/6.2011-766)
- Glezer A, Amitay M (2002) Synthetic jets. *Annu Rev Fluid Mech* 34:503–529
- Gnemmi P, Rey C, Eichhorn A, Bastide M, Striby J-L (2013) Pressure, temperature and free-flight projectile-displacement measurements during a plasma discharge generated on a supersonic projectile. *Int J Aerodyn* 3(1/2/3):84–104
- Grossman KR, Cybyk BZ, VanWie DM (2003) SparkJet Actuators for Flow Control. 41st Aerospace Sciences Meeting and Exhibit. doi:[10.2514/6.2003-57](https://doi.org/10.2514/6.2003-57)
- Haack SJ, Taylor T, Emhoff J, Cybyk B (2010) Development of an analytical SparkJet model. 5th AIAA Flow Control Conference. doi:[10.2514/6.2010-4979](https://doi.org/10.2514/6.2010-4979)
- Kalra C, Zaidi S, Alderman B, Miles R, Murt Y. (2007) Magnetically driven surface discharges for shock-wave induced boundary-layer separation control. 45th AIAA Aerospace Sciences Meeting and Exhibit. doi:[10.2514/6.2007-222](https://doi.org/10.2514/6.2007-222)
- Kalra CS, Zaidi SH, Shneider MN, Miles RB (2009) Shockwave induced turbulent boundary layer separation control with plasma actuators. 47th AIAA Aerospace Sciences Meeting Including the New Horizons Forum and Aerospace Exposition. doi:[10.2514/6.2009-1002](https://doi.org/10.2514/6.2009-1002)
- Kumar V, Alvi FS (2009) Toward understanding and optimizing separation control using microjets. *AIAA J* 47(11):2544–2557
- Kumar R, Ali MY, Alvi FS, Venkatakrishnan L (2011) Generation and control of oblique shocks using microjets. *AIAA J* 49(12):2751–2759
- Narayanaswamy V, Raja L, Clemens N (2010) Characterization of a high-frequency pulsed-plasma jet actuator for supersonic flow control. *AIAA J* 48(2):297–305. doi:[10.2514/1.41352](https://doi.org/10.2514/1.41352)
- Narayanaswamy V, Raja L, Clemens N (2012) Control of unsteadiness of a shock wave/turbulent boundary layer interaction by using a pulsed-plasma-jet actuator. *Phys Fluids*. doi:[10.1063/1.4731292](https://doi.org/10.1063/1.4731292)
- Popkin SH (2014) One-dimensional analytical model development of a plasma-based actuator. Dissertation, University of Maryland
- Popkin SH, Cybyk BZ, Land HB III, Foster CH, Emerick TM II, Alvi FS (2013) Recent performance-based advances in sparkJet actuator design for supersonic flow applications 51st Aerospace Sciences Meeting AIAA-2013-0322
- Reedy T, Kale N, Dutton J, Elliott G (2013) Experimental characterization of a pulsed plasma jet. *AIAA J* 51(8):2027–2031. doi:[10.2514/1.J052022](https://doi.org/10.2514/1.J052022)
- Samimy M, Kearney-Fisher M, Kim J, Sinha A (2011) High speed and high reynolds number jet control using arc filament plasma actuators for noise mitigation and for flow and noise diagnostics. 49th AIAA Aerospace Sciences Meeting Including the New Horizons Forum and Aerospace Exposition. doi:[10.2514/6.2011-22](https://doi.org/10.2514/6.2011-22)
- Shang JS, Kimmel RL, Menart J, Surzhikov ST (2008) Hypersonic flow control using surface plasma actuator. *J Propuls Power* 24(5):923–934
- Topolski M, Arora N, Ali M, Solomon J, Alvi F (2012) Experiments on resonance enhanced pulsed microjet actuators in supersonic cross flow. 6th AIAA Flow Control Conference. doi:[10.2514/6.2012-2813](https://doi.org/10.2514/6.2012-2813)
- Wang J, Choi K, Feng L, Jukes T, Whalley R (2013) Recent developments in DBD plasma flow control. *Prog Aerosp Sci*. doi:[10.1016/j.paerosci.2013.05.003](https://doi.org/10.1016/j.paerosci.2013.05.003)
- Webb N, Clifford C, Samimy M (2013) Control of oblique shock wave/boundary layer interactions using plasma actuators. *Exp Fluids* 54:1545. doi:[10.1007/s00348-013-1545-z](https://doi.org/10.1007/s00348-013-1545-z)
- Zhuang N, Alvi FS, Alkisar MB, Shih C (2006) Supersonic cavity flows and their control. *AIAA J* 44(9):2118–2128